Acta Materialia 188 (2020) 203–214

Contents lists available at ScienceDirect

Acta Materialia

journal homepage: www.elsevier.com/locate/actamat

Full length article

The interaction of deformation twins with long-period stacking ordered precipitates in a magnesium alloy subjected to shock loading

Fan Zhang[a,1], Yu Ren[b,c,1], Zhiqing Yang[d,1], Huhu Su[d,1], Zhen Lu[e], Chengwen Tan[c,*], Hailong Peng[f], Kentaro Watanabe[a], Bin Li[g], Matthew R. Barnett[h], Mingwei Chen[a,i,*]

[a] WPI Advanced Institute for Materials Research, Tohoku University, Sendai 980-8577, Japan
[b] Institute for Advanced Materials, North China Electric Power University, Beijing 102206, China
[c] School of Materials Science and Engineering, Beijing Institute of Technology, Beijing 100081, China
[d] Shenyang National Laboratory for Materials Science, Institute of Metal Research, Chinese Academy of Science, Shenyang 110016, China
[e] Mathematics for Advanced Materials Open Innovation Laboratory, AIST, 980-8577 Sendai, Japan
[f] Shcool of Materials Science and Engineering, Central South University, Changsha 410083, China
[g] Department of Chemical and Materials Engineering, University of Nevada, Reno, NV 89557, United States
[h] Institute for Frontier Materials, Deakin University, Pigdons Road, Geelong, Victoria 3216, Australia
[i] Department of Materials Science and Engineering, Johns Hopkins University, Baltimore, Maryland 21218, United States

ARTICLE INFO

Article History:
Received 26 September 2019
Revised 27 January 2020
Accepted 30 January 2020
Available online 5 February 2020

Keywords:
Magnesium alloy
Deformation twin
Long-period stacking ordered phase
Shock loading
Transmission electron microscopy

ABSTRACT

We report atomic-scale observations on the interaction of $\{10\bar{1}2\}$ deformation twins with 14H long-period stacking ordered (LPSO) phase in a magnesium alloy. It was found that the interaction strongly depends on the thicknesses of LPSO plates as well as the thickness ratios between LPSO plates and twins. We observed three size-dependent structure responses of LPSO to incoming twins: (1) pure shearing of thin LPSO plates in line with the incursive $\{10\bar{1}2\}$ twins; (2) twin-to-dislocation 'switch' from the alpha-Mg matrix to LPSO when LPSO/twin thickness ratios are below a critical value of 0.17 ± 0.01; and (3) elastic deformation of LPSO to accommodate the propagation of incoming twin when LPSO/twin thickness ratios are larger than 0.17 ± 0.01. Moreover, the inter-plate spacing of LPSO also influences the propagation modes of twins by controlling nucleation sites of new twins. These size-dependent interactions are accomplished by local structural transition of face-centered cubic units of LPSO during thin plate shearing and formation of gliding dislocations during LPSO deformation and twin blocked. The atomic-scale observations provide fundamental insights into these interaction modes and, hence, the precipitation strengthening mechanisms in Mg alloys under both quasi-static and dynamic loadings.

1. Introduction

The development of high strength Mg alloys has received extensive attentions due to the increasing demands of lightweight materials for energy-efficient and green environmental applications [1]. Precipitation strengthening is an important and effective approach to improve the strength of Mg alloys [2,3]. Among all known precipitates, long-period stacking ordered (LPSO) phases have been found highly effective in strengthening Mg-transition metal (TM)-rare-earth (RE) alloys [4,5]. Different from conventional face-centered cubic (fcc) and body-centered cubic (bcc) metals in which precipitation strengthening mainly results from interaction between dislocations and precipitates, twining is one of the dominant deformation modes of hexagonal close-packed (hcp) Mg alloys. Therefore, the interaction between deformation twins and precipitates plays a critical role in the precipitation strengthening and thereby the quasi-static and dynamic mechanical properties of Mg alloys [6–9]. For applications, the lightweight and high-strength Mg alloys are sought-after materials in fields such as military, automotive, aerospace and sporting goods, which require the understanding of the micro-mechanisms of deformation over a large range of strain rates. Since high strain rates promote the formation of deformation twins [7–9], the interactions between deformation twins and precipitates are more significant in Mg alloys under shock loading in comparison with quasi-static loading conditions. In addition to the importance for practical applications, the shock-loaded LPSO-reinforced Mg alloys are an ideal model system to study the twin-precipitate interactions.

Several twinning modes have been observed and reported in Mg and its alloys. Among them, $\{10\bar{1}2\}\langle 10\bar{1}1\rangle$ twining is the predominant mode and can be easily activated during deformation due to the low critical stress [6,8]. This type of twinning can accommodate the extension along the *c*-axis of the hexagonal lattice but not the

* Corresponding authors.
E-mail addresses: tanchengwen@126.com (C. Tan), mwchen@jhu.edu (M. Chen).
[1] These authors contributed equally to this work.

https://doi.org/10.1016/j.actamat.2020.01.064
1359-6454/

contraction along the *c*-axis. The shrinkage of $\{10\bar{1}2\}$ twins can occur under unloding or reversed loading, corresponding to the so-called detwinning [10,11]. A twinning process consists of twin nucleation, propagation and growth [12–14] and precipitates may act as obstacles and impede twin propagation and growth [15–16]. It can be expected that the interaction of $\{10\bar{1}2\}$ twins with precipitates significantly influences the yield strength, yield anisotropy and tension-compression asymmetry and formability of high strength Mg alloys [12,17]. Therefore, the interest in twin-precipitate interaction has been growing [18–21]. Transmission electron microscopy (TEM) and computer simulations have been extensively employed to investigate twin-precipitate interactions in various Mg alloys. Diffraction contrast imaging (bright-field (BF) and dark-field (DF) TEM) and selected area electron diffraction (SAED) suggest that there are mainly three types of interactions between $\{10\bar{1}2\}$ twins and precipitates in Mg-Al [15,22–23], Mg-Zn [24–26] and Mg-RE [27–32] alloys under quasi-static loading: (1) twins are held up by large precipitates and may continue by the nucleation of a twin in the matrix on the opposite side of the precipitates [15]; (2) precipitates are partly or fully engulfed by propagating twins but not sheared inside the twin [15,18,23,25]; and (3) precipitates become engulfed and sheared by the twins [30]. These enlightening results demonstrate the complexity and diversity of the nano-scale crystal defect-precipitate interactions in the hcp alloys. However, the underlying mechanisms of the multiplicity have not been well understood and, in particular, atomic-scale details of the twin/precipitate interactions in Mg alloys, illustrated by experimental observations, are still missing, despite the fact that extensive computational simulations and numerical calculations have been reported [21,33,34]. Apparently, the atomic-scale experiments are essential for in-depth understanding of the precipitation strengthening in hcp crystals and, as the benchmarks, for theoretical modeling. Moreover, there is a shortage of investigations on the effect of high deformation rates on the twin/precipitate interactions in precipitation hardening Mg alloys under shock loading in spite of the technical importance of this subject [35–37].

In this study, we investigated the interactions of $\{10\bar{1}2\}$ deformation twins with 14H LPSO plates in a $Mg_{97}Zn_1Y_2$ (at.%) alloy using a spherical abreaction corrected scanning transmission electron microscope (STEM) equipped with a high-angle annular dark field detector (HAADF). The atomic-scale characterization reveals the size-dependent structure responses of LPSO to incoming twins by pure shearing, twin-to-dislocation 'switch' and elastic deformation.

2. Experimental procedures

The material used in the present study is a $Mg_{97}Zn_1Y_2$ (at.%) alloy. This alloy was prepared from high purity (99.9 wt.%) Mg, (99.9 wt.%) Zn and Mg-25 wt.% Y master alloy by high frequency induction melting under Ar atmosphere. The cast alloy was heat-treated at 500 °C for 2 h and followed by water quenching. Samples used for shock loading compression tests were cut from the solution treated ingot. "Soft" shock recovery was conducted using a 57 mm single gas gun with systematic control of the experimental loading parameters and design shock fixtures of the soft shock recovery experiments. These factors are crucial for recovering the test samples with precisely controlled loading history and a minimal residual strain. They are also important for correctly assessing the influence of shock wave deformation on the structure and properties of the material [38,39]. The residual plastic strain of shock-loaded recovery samples measured by an outside micrometer is less than 2%, indicating that the lateral release waves on the recovery sample is negligible. The detail experimental procedures were reported in our previous paper [40]. The thickness of Mg flyer plate was 3.2 mm to generate a pulse with the duration of 1.2 μs and shock loading to 4 GPa was accomplished with the projectile traveling velocity of 874 m s^{-1}.

The microstructure of shock-loaded samples was characterized by scanning electron microscopy (SEM) and transmission electron microscopy (TEM). For electron back-scattered diffraction (EBSD) mapping, samples were electropolished in a chemical solution with 20. vol% nitric and 80. vol% ethanol at a voltage of 15 V. EBSD was performed using a Zeiss Ultra 55 field-emission SEM equipped with HKL data acquisition software. TEM samples were sliced as 0.5 mm sheets along the direction parallel to the shock loading direction. The slices were gently ground to ~ 200 μm thick for twin-jet electropolishing in a 10. vol% nitric acid and 90. vol% ethanol using Struers TenuPol-5 twin-jet polisher. Gentle ion milling was used to clean the electrochemically polished samples. STEM observations were performed using a spherical aberration-corrected JEOL JEM-2100F TEM operating at 200 kV. HAADF-STEM images were acquired using a HAADF detector with the collection angles ranging from 100 to 267 mrad. BF-STEM was acquired simultaneously by a Gatan BF detector, which was used for taking the diffraction-contrast images of twins. The original atomic-resolution HAADF-STEM images were filtered by HRTEM Wiener filter using Gatan Digital Micrograph to reduce the noisy contrast [41].

3. Results

3.1. Microstructures of $Mg_{97}Zn_1Y_2$ alloy before and after shock loading

The microstructure of the $Mg_{97}Zn_1Y_2$ alloy is composed of the interdendritic LPSO phases and α-Mg grains as shown in Fig. 1(a), which has been reported before [40]. Inside the α-Mg grains, a high density of LPSO plates can be observed (Fig. 1(b)). The precipitates are enriched with Y and Zn and show the bright contrast in HAADF-STEM images. The length direction of LPSO plates is parallel to the basal plane trace, resulting in the formation of a lamella structure. Fig. 1(c) illustrates a high-resolution HAADF-STEM image of the LPSO precipitate from the region, as marked by the black rectangular frame in Fig. 1(b). The atomic-resolution image includes seven building blocks of LPSO. There are two bright atomic layers with enriched Y and/or Zn in each building block. Two adjacent building blocks have the opposite stacking sequences of the closed packed planes. One is an ABCA-type fcc block and the other is ACBA-type defective fcc block. The two adjacent building blocks, together with the three α-Mg atomic layers between them, constitute a unit cell 14H-type LPSO structure [42,43].

Few twins are observed in samples subjected to quasi-static loading [29] or cold-rolling [44]. However, profuse $\{10\bar{1}2\}$ deformation twins are activated in the α-Mg matrix of the present $Mg_{97}Zn_1Y_2$ alloy subjected to shock loading as revealed by the EBSD mapping and quantitative misorientation analysis (see Fig. 2(a), (b) and (c)), which is in line with the fact that shock loading promotes twinning [7–9]. The presence of deformation twins in the shock-loaded samples was further verified by the TEM image and corresponding SAED pattern (Fig. 2(d)). The $\{10\bar{1}2\}$ twins "traverse" across multiple LPSO plates with different thicknesses and inter-plate spacing. Additionally, some 14H LPSO plates are partly embedded inside the $\{10\bar{1}2\}$ twins and the embedded parts are evidently deviated in response to the twin shearing. The microscopic observations of twin/precipitate interactions are similar to previous reports [15,22,28].

3.2. Interaction between $\{10\bar{1}2\}$ deformation twins and thin LPSO plates

Fig. 3a shows a $\{10\bar{1}2\}$ twin traversing a ~5 nm thick LPSO plate composed of three building blocks of 14H LPSO phase. This LPSO plate was partly engulfed by the twin and the interaction leads to the local twin boundary deviating from the original $\{10\bar{1}2\}$ twinning plane, as indicated by the dashed line in Fig. 3(b). Fig. 3(c) is a HAADF-STEM image taken from the intersection region of the twin and LPSO (region I_1 in Fig. 3(b)), showing that a prismatic-basal (PB) interface, at which

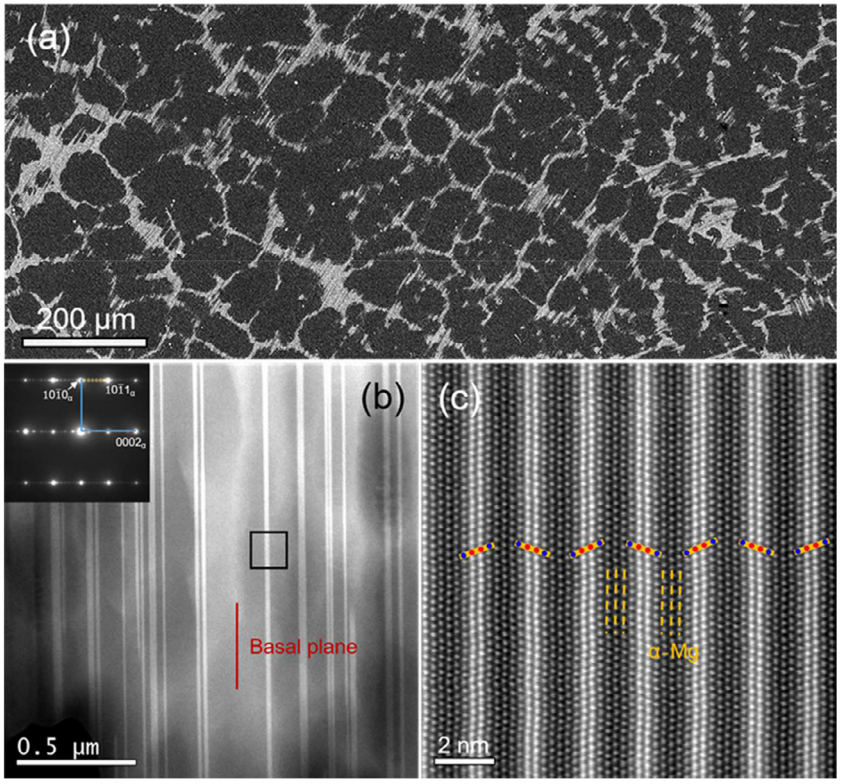

Fig. 1. (a) SEM image showing the α-Mg grains and interdendritic LPSO phases. (b) A low-magnification HAADF-STEM image showing the thin and thick LPSO precipitates inside the α-Mg matrix. The inset is the corresponding selected area diffraction (SAED) pattern. (c) High-resolution HAADF-STEM image taken from the marked region in (b) showing the atomic structure of the LPSO phase. The two adjacent building blocks, together with the three α-Mg atomic layers between them, constitute a unit cell of the 14H LPSO.

the prismatic plane in the twin is approximately parallel to the basal plane of the matrix, is formed at the LPSO/twin boundary. The closed circuit in the dichromatic complex shown in Fig. 3(d) indicates that the PB interface exhibits a periodic character ($15d^{\mu}_{\{10\bar{1}0\}} = 16d^{\lambda}_{\{0001\}}$). There are misfit dislocations at the PB interface due to the lattice difference between prismatic and basal planes ($c^{\lambda}_{Mg} \neq \sqrt{3}/2a^{\mu}_{Mg}$) [45–48]. The schematic diagram in Fig. 3(e) shows one misfit dislocation within one pseudo-period at the PB interface. In addition, the lattice mismatch at the PB/basal-prismatic (BP, the basal plane in the twin is nearly parallel to the prismatic plane in the matrix) boundary is approximately 6.5% [45–48], which is also relieved by misfit dislocations at the PB/BP interface [49–51]. The interfacial defects at the twin/LPSO interface were characterized by using the circuit mapping method in the dichromatic complex based on the interfacial defect theory [51,52]. The circuits numbered by "1", "2" and "3" in the HAADF-STEM image shown in Fig. 3(c) were drawn by following the same trace overlapped on the dichromatic complex for BP/PB interface (Fig. 3(d)) in α-Mg.

The resulting dislocations during twin-LPSO interaction can be well illustrated by Thompson hexahedron (Fig. 4). When the incident electron beam is parallel to ***AB***, 60° ⟨**a**⟩ dislocation with vector ***AC*** or ***BC*** and screw ⟨**a**⟩ dislocations with vector ***AB*** are designated as ⟨$\mathbf{a}_{60}$⟩ and ⟨$\mathbf{a}_s$⟩ (Fig. 4(a)), respectively. The partial dislocation with vector ***Aα*** or ***Bα*** deviates 30° from the dislocation line and the partial dislocation with vector ***Cα*** is perpendicular to the dislocation line, which represents 30° and 90° partials (Fig. 4(a)), respectively. Fig. 4(b) illustrates the schematic diagram showing the Burgers vector of perfect ⟨**c**⟩ (***BB₀*** or ***CC₀***), ⟨$\boldsymbol{c}+\mathbf{a}_{60}$⟩ (***AC₀*** or ***CB₀***), and ⟨$\boldsymbol{c}+\mathbf{a}_s$⟩ (***AB₀***) dislocations in the hcp structure, which will be discussed in detail in Section 4.2. The closure failures of the Burgers circuits "2" and "3" in Fig. 3 indicate the presence of two basal ⟨$\mathbf{a}_{60}$⟩ dislocations along the bottom fcc sublayer within two consecutive pseudo-periodicities in regions at the PB interface. The basal ⟨**a**⟩ dislocations are evidently produced by the twin/LPSO interaction.

Fig. 5(a) shows an atomic-resolution HAADF-STEM image of region I_2 in Fig. 3(b), revealing that the original building blocks of the LPSO and the ABCA-stacked structure have transformed into a hcp structure during the twin/LPSO interaction. The circuits in the dichromatic complexes for BP/PB interfaces shown in Fig. 5(b), (c) and (d) were drawn by following the same traces numbered "1", "2" and "3" in the HADDF-STEM image (Fig. 5(a)). Closure failures of the circuits suggest that there are crystal dislocations and misfit dislocations at the interface of deformed and pristine regions of the LPSO plate. The Shockley partials of building block "1" and "2" at the interface are 90° (***Cα***) partial dislocations, while it is a 30° (***Aα*** or ***Bα***) partial dislocation of building block "3" at the interface. In addition, there are misfit dislocations in regions "2" and "3", and a perfect basal ⟨**a**⟩ dislocation in region "3", according to the closure failures shown in Fig. 5(c) and (d). The basal ⟨**a**⟩ dislocation can also be observed at the upper-right PB interface, as indicated by "⊥" in Fig. 5(a).

Fig. 6 shows an atomic-resolution image recorded from intersection region between the twin and LPSO plate (II indicated in Fig. 3 (a)). The shearing of LPSO phase caused by twinning can be observed again. The twin-LPSO interface is composed of alternative BP and PB facets, which are perpendicular to each other with a length ranging from 1.5 nm to 2 nm. The circuits in the dichromatic complexes for BP/PB interfaces (Fig. 6(b), (c) and (d)) were drawn by following the same traces numbered "1", "2" and "3" overlapped on the HAADF-STEM image (Fig. 6(a)), respectively. Closure failures of the circuits indicate that there are crystal dislocations and misfit dislocations at the interface between the deformed and pristine regions of this LPSO plate. The Burgers vector at the PB/BP facet surrounded by circuit "1" is a result of the combination of one basal ⟨$\mathbf{a}_{60}$⟩ dislocation, a 30° partial, as shown in Fig. 6(b). The crystal dislocations at facet "2", "3" are

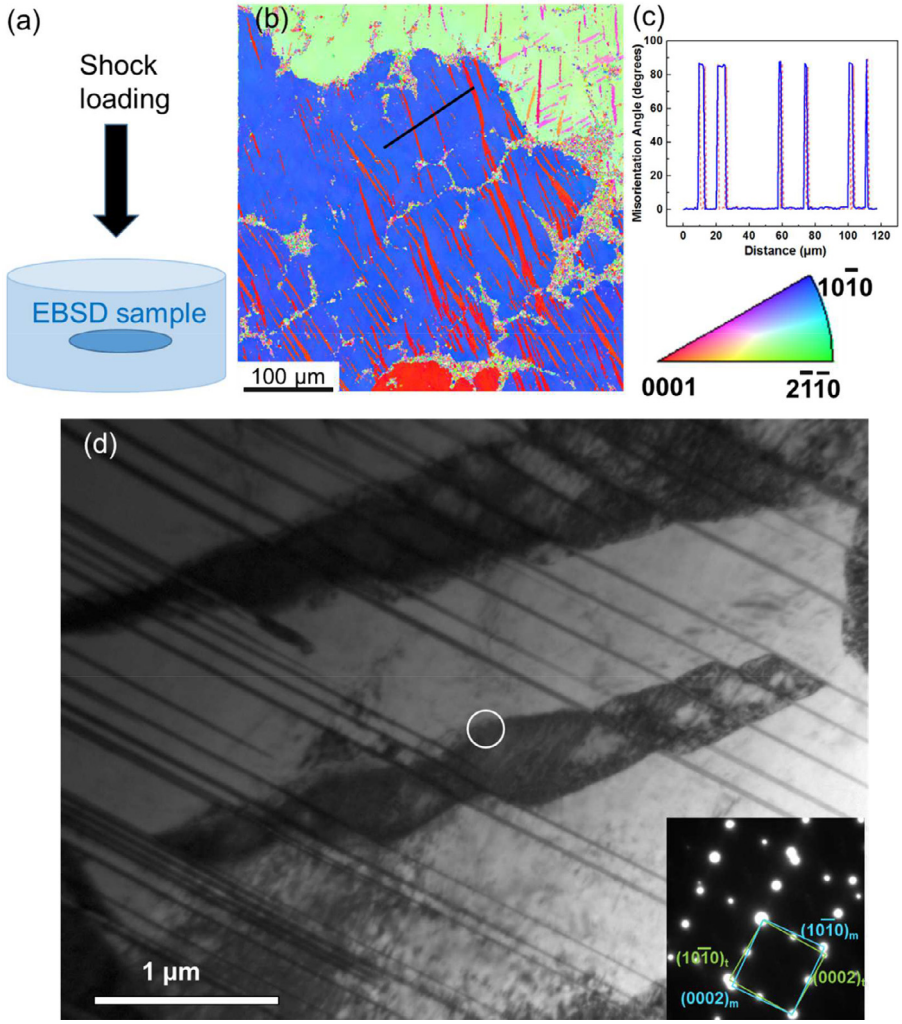

Fig. 2. (a) Schematic diagram showing the normal direction of EBSD sample parallel to the shock loading direction. (b) EBSD inverse pole image showing profuse $\{10\bar{1}2\}$ twins in the shock-loaded sample. (c) Point-to-point misorientation (red line) and point-to-origin misorientation (blue line) profiles along the line indicating the occurrence of $\{10\bar{1}2\}$ twin in region marked by the black bar. (d) TEM image showing the $\{10\bar{1}2\}$ twins transmitting through LPSO plates with varying thicknesses and inter-plate spacing. The inset is the corresponding SAED pattern taken from the circular area that demonstrates the $\{10\bar{1}2\}$ twin. (For interpretation of the references to colour in this figure legend, the reader is referred to the web version of this article.)

a 30° partial and a basal $\langle \mathbf{a_{60}} \rangle$ and a 30° partial, respectively. There are misfit dislocations at BP/PB facets "2" and "3".

3.3. *Interaction between $\{10\bar{1}2\}$ twins and thick LPSO plates*

Fig. 7(a) shows a deformation twin impinging upon a 14H LPSO plate composed of five building blocks. The incoming twin only partially contacts with the LPSO plate and an obvious gap between the twin and LPSO can be seen. Note there is inhomogeneous strain contrast within the LPSO plate, marked by the white box, in the vicinity of the incoming twin frontier. Higher magnification HAADF-STEM imaging (Fig. 7(b)) reveals that the structure of the LPSO is retained, in contrast with the shearing of thin LPSO plates by deformation twins in Figs. 5 and 6. The inhomogeneous strain contrast in the LPSO plate (Fig. 7(a)) corresponds to the slip steps with a height of two-basal-layers in each of the five building blocks, indicating that the LPSO plate experienced plastic deformation by dislocation glide. These steps could be produced by a $\langle c+a \rangle$ dislocation which glides through the LPSO plate as reported previously [53].

At the atomic scale (Fig. 7(c)), the front tip of the twin is seen to directly impinge on the LPSO segment, leading to the formation of a distinct twin/LPSO interface. Most significantly, a step is generated in the first building block close to the twin/LPSO interface, suggesting that a lattice dislocation is generated and glide through the LPSO plate during the direct twin-LPSO interaction. Fig. 7(d) further shows steps due to the gliding of $\langle c+a \rangle$ dislocations as evidenced by drawing Burgers circuits following the trace shown in Fig. 7(c). The dislocations bounding with one broken building block at each step are 30° Shockley partials and the two partials in the same step have opposite signs. Hence, $\{10\bar{1}2\}$ twins are seen to 'traverse' across 14H LPSO plates composed of five building blocks via a twin-to-dislocation 'switch' from the α-Mg matrix to LPSO.

The interaction of a $\{10\bar{1}2\}$ twin with a relatively thick LPSO plate composed of eight building blocks is displayed in Fig. 8. The part of LPSO plate embedded inside of the deformation twin is marked by the arrow in Fig. 8(a) and imaged by high-resolution HAADF-STEM (Fig. 8(b)). It can be seen that the LPSO segment displays steps caused by the gliding dislocations. In addition to steps with a two-basal-layers height as a result of the slip of a $\langle c+a \rangle$ dislocation within the LPSO, a step with a three-basal-layers height was also found. Interestingly, two groups of steps with two-basal-layers height on the right side of Fig. 8(b) were observed in the fifth building block but disappeared in the sixth building block of LPSO plate. Burgers circuit surrounding two adjacent steps shows no close failure in the fourth building block but closure failure in the fifth building block displays a

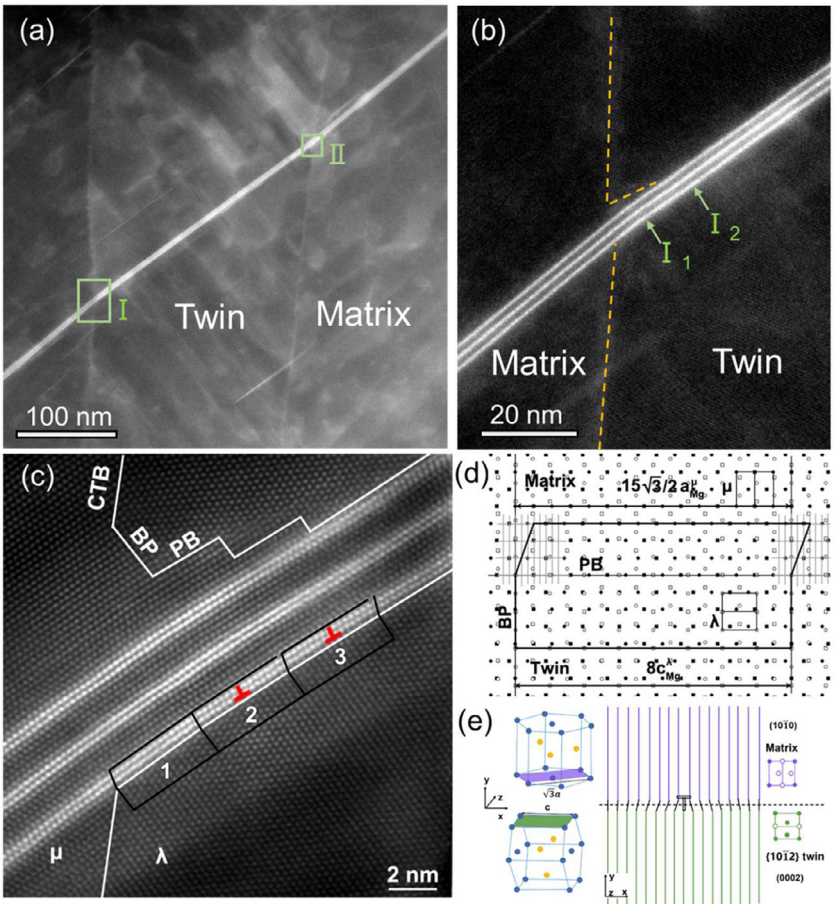

Fig. 3. (a) Low-magnification HAADF-STEM image showing the twin transmitting through the thin plate composed of three building blocks of 14H LPSO. (b) A magnified HAADF-STEM image taken from the region I. (c) Misfit dislocations within a pseudo-periodic structure (every 16 basal planes or 15 prismatic planes) along the PB facet obtained from the region I_1 in (b). The closure failure of the Burgers circuits in regions 2 and 3 showing the basal ⟨**a**⟩ dislocations at the PB interface. (d) The circuit shown in the dichromatic complex for a {10$\bar{1}$2} BP/PB interface was drawn by following the same trace (numbered "1") overlapped on the HADDF-STEM image. (e) Schematic illustration of a misfit dislocation at the PB interface. (For interpretation of the references to colour in this figure legend, the reader is referred to the web version of this article.)

basal ⟨$\mathbf{a_{60}}$⟩ dislocation (Fig. 8(c)). The details of the deformation mode of LPSO will be discussed in detail in Section 4.2.

3.4. Interaction between narrow {10$\bar{1}$2} twins and thick LPSO plates

Fig. 9 shows a narrow {10$\bar{1}$2} deformation twin interacting with a thick LPSO plate consisting of twelve building blocks. It appears that the incoming twin is fully stopped in front of the LPSO plate as presented in Fig. 9(a), which is further verified by a noticeable α-Mg matrix gap between the incoming twin and the LPSO plate (Fig. 9(b)). Additionally, there is an α-Mg matrix gap between the LPSO plate and the outgoing twin. The shortest gap marked by the rectangle (Fig. 9(b)) between the incoming twin and LPSO plate is equal to five α-Mg basal layers (Fig. 9(c)). No dislocation glide can be observed within the LPSO plate sandwiched between the incoming and outgoing twins, suggesting that the elastic deformation of this LPSO plate accommodates the twin propagation. This is consistent with previous suggestions that twining may lead to elastic deformation of precipitates in Mg alloys [15,16,18,54]. The nucleation of an outgoing twin on the other side of LPSO plate appears to be activated by the elastic strains at the LPSO/α-Mg interface, which are generated by the elastic deformation of LPSO.

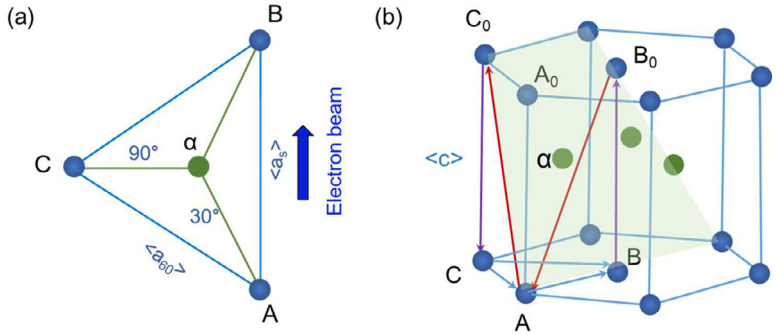

Fig. 4. (a) Schematic diagram showing the Burgers vectors of basal 60° ⟨**a**⟩ (***AC*** or ***BC***), screw ⟨**a**⟩ (***AB***), 30° (***Aα*** or ***Bα***) partial and 90° (***Cα***) partial dislocations in the hcp structure. Basal 60° ⟨**a**⟩ and screw ⟨**a**⟩ dislocations are denoted as ⟨$\mathbf{a_{60}}$⟩ and ⟨$\mathbf{a_s}$⟩, respectively. Vector ***AB*** displays that the view direction of 1/3[1$\bar{2}$10] for atomic-resolution observations in the present study. (b) Schematic diagram showing the Burgers vectors of perfect ⟨**c**⟩ (***BB$_0$*** or ***CC$_0$***), ⟨$\mathbf{c+a_{60}}$⟩ (***AC$_0$*** or ***CB$_0$***), and ⟨$\mathbf{c+a_s}$⟩ (***B$_0$A***) dislocations in the hcp structure.

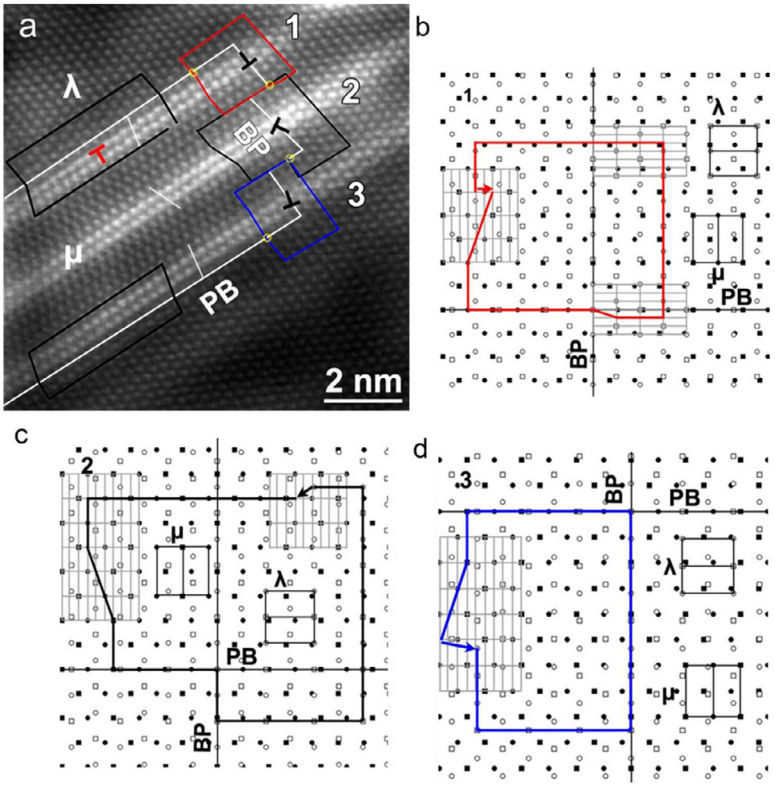

Fig. 5. (a) Atomic-resolution HAADF-STEM image, taken from region I_2 indicated in Fig. 3b, showing the shearing of LPSO phase by a {10$\bar{1}$2} twin. The Burgers circuits were drawn along the right-handed screw and edge dislocation lines with positive line sense pointing out of the paper. The basal ⟨$\mathbf{a_{60}}$⟩ dislocation distributes at the left-upper PB interface. The dislocations at BP/PB facets "1", "2" and "3" in the dichromatic complexes are (b) a 90° partial dislocation, (c) a 90° partial dislocation, and (d) one basal ⟨$\mathbf{a_{60}}$⟩ and a 30° partial dislocations, respectively.

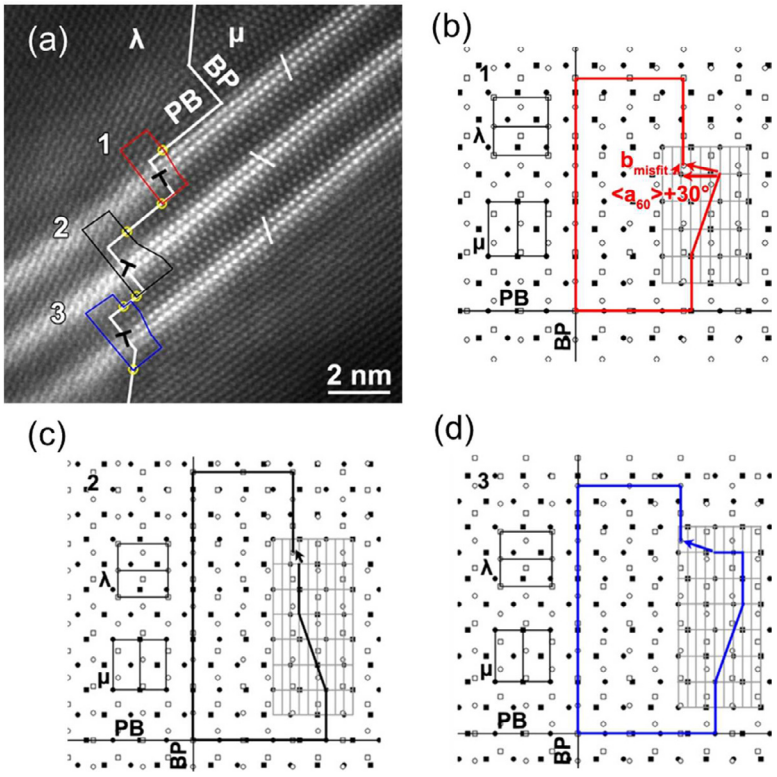

Fig. 6. (a) Atomic-resolution HAADF-STEM image taken from the marked region II in Fig. 3a showing the shearing of LPSO phase by a {10$\bar{1}$2} twin. The circuits shown in the dichromatic complexes for {10$\bar{1}$2} BP/PB interfaces were drawn by following the same traces numbered "1", "2" and "3" overlapped on the HADDF-STEM image. The dislocations at the facet 1, 2, 3 are composed of (b) one basal ⟨$\mathbf{a_{60}}$⟩ and a 30° partial dislocations, (c) a 30° partial dislocation, and (d) one basal ⟨$\mathbf{a_{60}}$⟩ and a 30° partial dislocations, respectively. (For interpretation of the references to colour in this figure legend, the reader is referred to the web version of this article.)

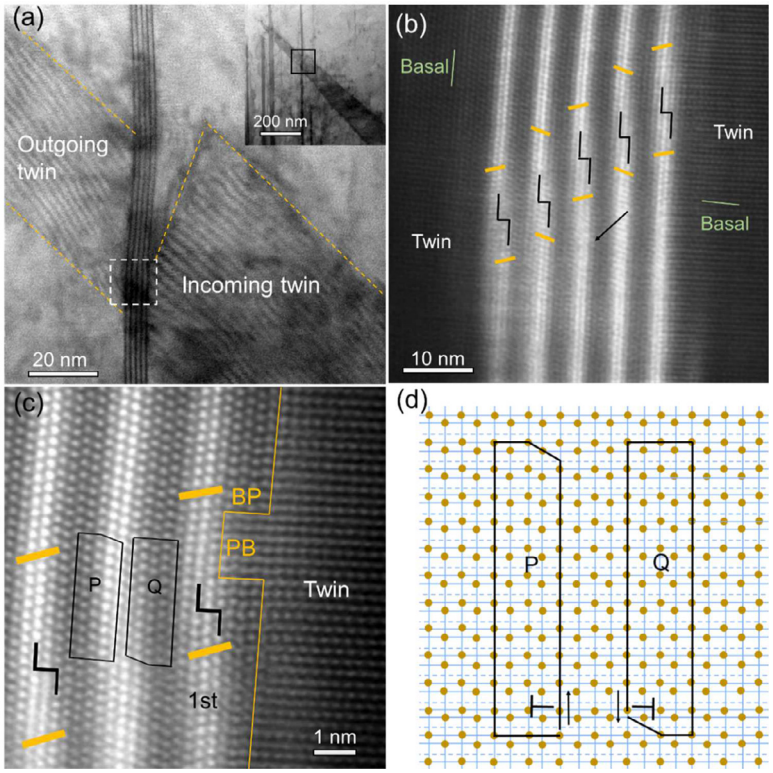

Fig. 7. (a) BF-STEM image showing a $\{10\bar{1}2\}$ twin interacting with the 14H LPSO plate composed of five building blocks. Inset: low-magnification image of a $\{10\bar{1}2\}$ twin interacting with LPSO plates. (b) HAADF-STEM image taken from the marked region in (a) showing slip steps along each of the five building blocks within the LPSO plate. (c)Atomic-resolution HAADF-STEM image showing the slip step. The step generated in the first building block of LPSO is very close to the tip of the twin. (d) Burgers circuits around steps shown in (c).

Fig. 10 presents the interaction of a $\{10\bar{1}2\}$ twin with two adjacent thick LPSO plates with an inter-plate spacing of 10 nm. The incoming twin is fully stopped in front of the first LPSO plate and continues to propagate on the opposite side of the second LPSO plate (Fig. 10(a)). An obvious misalignment between the incoming and outgoing twins suggests that the outgoing twin is independent from the incoming twin and formed by a new nucleation event. Interestingly, there is no twin trace in the 10 nm thick α-Mg slat sandwiched between the two LPSO plates. This result was further examined by the atomic-resolution HAADF-STEM of rectangle regions "b", "c" and "d". There is a PB interface which is 3 basal α-Mg layers away from the LPSO/α-Mg interface on both outsides of the sandwich-like structure (Fig. 10(b) and (d)), similar to the case of a twin interacting with a single thick LPSO plate (Fig. 9). Moreover, no twins can be seen in the sandwiched α-Mg slats with the thickness of 10 and 20 nm (Supplementary Fig. S1a-e). During this deformation process, the sandwiched α-Mg slat together with the two adjacent LPSO plates are elastically deformed to accommodate the incoming twinning shear. However, a deformation twin is observed in a ~70 nm thick α-Mg slat sandwiched between two thick LPSO plates (Supplementary Fig. S1g), indicating that the stiffness of the sandwiched α-Mg slat cannot stand for pure elastic deformation when the slat thickness is larger than a critical value, presumably the critical size of a twin nucleation.

4. Discussion

In our atomic-scale HAADF-STEM study we observed three deformation modes by which propagating $\{10\bar{1}2\}$ twins traverse LPSO plates in their paths: (1) the propagation of a twin is accommodated by shearing of a thin coherent LPSO plate (Mode-I); (2) a twin transmits through a LPSO plate via the dislocation glide (Mode-II); and (3) an incoming twin is fully stopped by a thick LPSO and a new twin nucleates at the opposite side of LPSO/ α-Mg interface accompanied by elastic deformation of LPSO (Mode-III). In this section, we will discuss the mechanisms of three deformation modes and the controlling factors of these modes.

4.1. The twin directly transmits through the LPSO plate by shearing

On the basis of electron diffraction, the shear deformation of precipitates by twin shearing has been suggested in Mg-Zn-Gd alloys [30]. However, detailed structural changes of the twinned LPSO phase remain unknown. The LPSO phase is composed of hcp-Mg units and Y/Zn rich building blocks with a local fcc stacking (Fig. 1) and, thereby, can be regarded as a lamellar structure with alternate hcp and fcc layers. In our atomic-scale observations, it was found that the local fcc units convert into the hcp structure to facilitate the twin propagation as a $\{10\bar{1}2\}$ twin shears the LPSO phase. Upon shearing, basal $\langle\mathbf{a}\rangle$ dislocations distribute at the alternative BP and PB interfaces (Figs. 5 and 6), and glide along the LPSO plate (Figs. 3 and 5). As a result, the sheared 14H LPSO segments possess the same crystal structure and crystallographic orientation as the incursive $\{10\bar{1}2\}$ twin. In contrast, the random distribution of basal $\langle\mathbf{a}\rangle$ dislocations within the LPSO results in local lattice bending (Fig. 3).

Based on the atomic-scale observations, the local structural transition of the FCC units in the 14H LPSO phase by twin shearing exhibits similar features of the classical fcc-hcp martensitic phase transformation [55]. This phase transformation is accomplished by the gliding of Shockley partial dislocations at glissile interfaces, causing the receding lattice of fcc structure to be sheared into the basal plane of hcp structure along $\langle 110\rangle$ [55]. In this study, 30° or 90° Shockley partial dislocations were observed at the BP/PB boundaries, which sit at the interfaces between the transformed and pristine LPSO phase segments (Figs. 5 and 6). In addition, the basal $\langle\mathbf{a}\rangle$ dislocations were generated in the fcc sublayers of LPSO phase and distributed at the BP/PB facets. Therefore, the dissociation, motion and reaction of these basal $\langle\mathbf{a}\rangle$ dislocations lead to the transformation of the local fcc lattice to

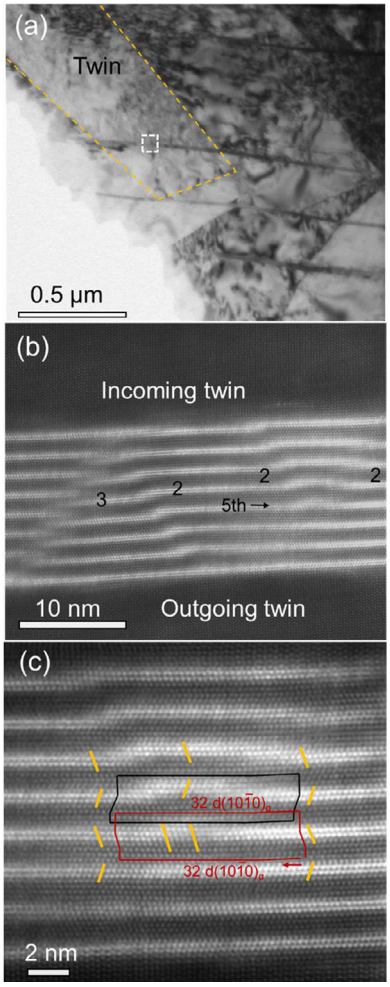

Fig. 8. (a) TEM image showing the interaction between deformation twins and thick LPSO plates. (b) HAADF-STEM image showing multiple slip steps generated in the LPSO plate. (c) Enlarged image of two groups of steps on the right side of (b). Burgers circuit surrounding the two adjacent steps showing no close failure in the fourth building block but closure failure showing a basal $\langle \mathbf{a_{60}} \rangle$ dislocation in the fifth building block.

the hcp structure together with the resultant dislocations at the PB/PB interfaces.

4.2. The twin traverses the LPSO plate via the glide of dislocations

When a propagating twin encounters with an interface (twin boundary, grain boundary (GB), precipitate/matrix interface), the concentrated shear stress at the twin front [56–58] can be relaxed by dislocation slip [59] or sequential twinning [58,60]. In the present study, when an incoming twin meets a thin LPSO plate, the twin shearing is accommodated by direct shear deformation of the LPSO plate (Figs. 5 and 6). When an incoming twin impinges upon a thicker LPSO plate, dislocation glide is initiated in LPSO plate, resulting in a 'switch' from twinning in α-Mg to dislocation glide in LPSO (Figs. 7 and 8).

The shear associated with the $\{10\bar{1}2\}$ twinning in hcp Mg has a $\langle c \rangle$ component and thus $\langle c+a \rangle$ dislocations with a $\langle c \rangle$ component are required to accommodate the shear strain. Emissary dislocations with a $\langle c+a \rangle$ Burgers vector have been observed at terminating twin tips [15,61–62]. As illustrated in Figs. 7 and 8, $\langle c+a \rangle$ dislocations are activated within the LPSO phase ahead of twin tips and glide across a 14H phase, leading to the formation of slip steps with a height of two-basal-layers. In addition, a step with three-basal-layers height can also be formed by the successive glide of one $\langle c+a \rangle$ dislocation and one dislocation with a $^1/_2 \langle c \rangle$ component.

The two-basal-layers high steps on the left and right sides in Fig. 8 (b) and (c) were produced by the glide of $\langle c+a \rangle$ dislocations on two different slip planes. The two dislocations can interact and react, leading to the formation of a $\langle \mathbf{a_{60}} \rangle$ dislocation in the fifth building block. Careful analysis indicates that only reaction of $\langle \boldsymbol{c+a_{60}} \rangle$ ($\boldsymbol{AC_0}$ or $\mathbf{B_0C}$ in Fig. 4(b)) and $\langle \boldsymbol{c+a_s} \rangle$ ($\mathbf{B_0A}$ in Fig. 4(b)) dislocations can result in the formation of $\langle \mathbf{a_{60}} \rangle$ dislocation while the reactions of two $\langle \boldsymbol{c+a_{60}} \rangle$ dislocations or two $\langle \boldsymbol{c+a_s} \rangle$ dislocations can be excluded. The reactions can be described as:

$$\boldsymbol{AC_0 + B_0A = AC + BA = BC} \ (<\mathbf{a_{60}}>) \quad (1)$$

$$\text{or } \boldsymbol{B_0C + AB_0 = BC + AB = AC} \ (<\mathbf{a_{60}}>) \quad (2)$$

In fact, the formed $\langle \mathbf{a_{60}} \rangle$ dislocation is composed of the 30° and 90° Shockley partial dislocations bounding the left and right steps in the fifth building block (Supplementary Fig. 2).

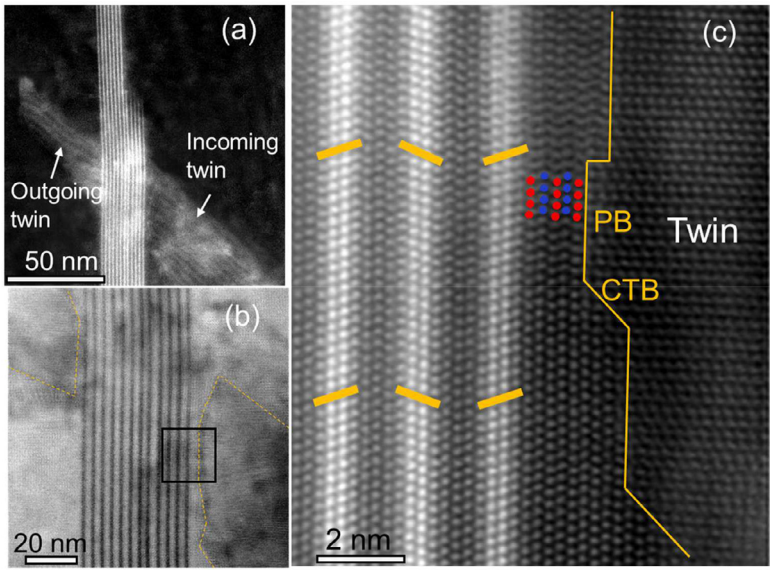

Fig. 9. (a) HAADF-STEM image showing a narrow twin arrested by a thick 14H LPSO plate composed of twelve building blocks. (b) BF-STEM image taken from the marked region in (a) showing the incoming twin is fully stopped in front of the LPSO plate. (c) Atomic-resolution HAADF-STEM image showing the nearest distance between the twin tip and LPSO plate is equal to five α-Mg basal layers.

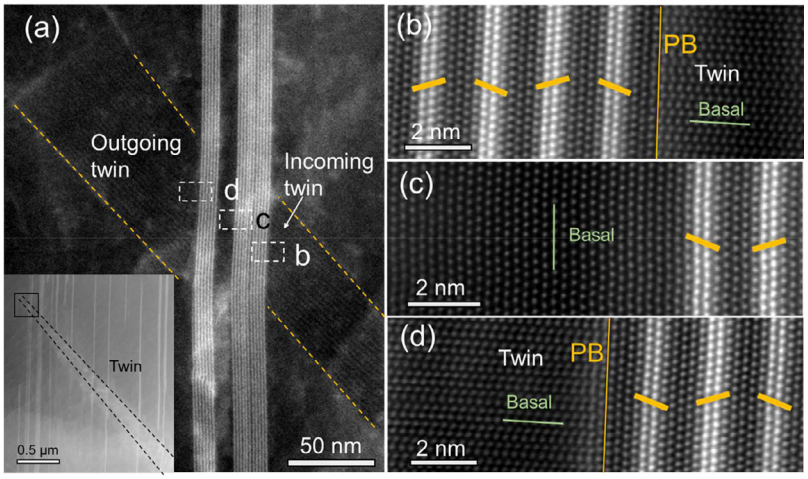

Fig. 10. (a) A twin transmitting across two thick LPSO phases with an inter-plate spacing of 10 nm. Inset: HAADF-STEM image showing the twin transmitting through several LPSO units and the high magnification image was taken from the region marked by rectangular in (a). (b) The incoming twin is arrested in front of the first LPSO plate. (c) No twins can be seen in the α-Mg slat sandwiched between two thick LPSO plates. (d) The outgoing twin nucleating at the far side of the α-Mg /LPSO interface of the second LPSO plate.

4.3. The elastic deformation of LPSO and the nucleation of a new twin

The propagation of an incoming twin can be fully terminated by a thick LPSO plate. The local shear stress concentration generated at the terminating twin front can evidently cause a new twin formation on the opposite side of the LPSO plate in the neighboring α-Mg matrix. In this case, it appears that the role of the precipitates is similar to GBs, except that the orientations of the matrix on both sides of the precipitates are the same, favoring the nucleation of a new twin with the same variant.

When the spacing of two adjacent LPSO plates is smaller than 20 nm, the thin α-Mg slat sandwiched between the two LPSO plates has an extraordinary stiffness and only deforms elastically during twin shearing (Fig. 10). However, twin shearing occurs in the α-Mg slat with a thickness of about 70 nm (Fig. S1g). These observations suggest that the inter-plate spacing of LPSO is also an important factor controlling the twin propagation. The effect of the inter-plate spacing for twinning may originate from the competition with the critical size for a twin embryo or the nano-size effect in strengthening, similar to the grain-size [9,63,64] and crystal-size dependence [65–68] of twinning. Certainly, thick LPSO precipitates can behave similarly as high-angle GBs when a deformation twin propagates the obstacles by the nucleation of a new twin on the opposite side of LPSO plates. Since the LPSO plates divide the α-Mg grain into many slats with different thicknesses, it may be speculated that the presence of thick LPSO phases can exert a similar role on the critical resolved shear stress for twinning in Mg as GBs.

4.4. Factors governing the interaction modes between twining and LPSO

Since the 14H LPSO and α-Mg matrix has a definite relation of $(0001)_{14H} \parallel (0001)_{\alpha-Mg}$, $[0\bar{1}10]_{14H} \| [\bar{1}\bar{1}20]_{\alpha-Mg}$, only one LPSO variant can be formed in each α-Mg grain. As for the $\{10\bar{1}2\}$ twins, there are six twin variants in a hcp structure, which can form three crystallographically different kinds of twin-LPSO interactions with the twinning directions along $\langle 10\bar{1}\bar{1}\rangle$ in a α-Mg grain with one LPSO variant, as shown in Supplementary Fig. 3a. With the determined crystallographic relations, the interaction angle between the basal LPSO precipitate and twining growth direction is always at ~43.1° (Supplementary Fig. 3b). Therefore, the $\{10\bar{1}2\}$ twin/LPSO interaction modes are crystallographically independent on orientations of the LPSO plates, twinning directions, grain orientations and the loading direction. The only factor that affects the interaction modes is the thicknesses of LPSO plates and thickness ratios between twins and LPSO plates.

For $\{10\bar{1}2\}$ twins interacting with LPSO plates, the thickness of LPSO plates along the [0001] direction and the thickness of incoming twins were acquired from HAADF-STEM images. Since both $\{10\bar{1}2\}$ twins and LPSO plates were imaged in the edge-on condition in the $\langle 1\bar{2}10\rangle$ zone-axis, their thicknesses can be determined from the atomic-resolution images by counting the number of unit cells of 14H LPSO and atomic layers of twins. We conducted over 30 atomic-scale measurements and characterizations from a wide range of LPSO plate thicknesses from ~1.8 nm to ~51 nm and twin band thicknesses from ~35 nm to ~606 nm. The quantitative analyses reveal three distinct regions of twin-LPSO interactions, which are marked different colors and separated by the black and purple dashed lines in Fig. 11(a). In the Model-I region, the LPSO plates experience twin shearing when the thickness is one to four building blocks, i.e. 1.8 nm-7 nm. We noticed that the twinning is always arrested regardless of the thickness of deformation twins when the thickness of LPSO plates is larger than five building blocks. The critical thickness of the 14H LPSO plates is denoted by the black dashed line in Fig. 11(a). With the increase of the LPSO plate thickness, dislocation glide mediated twining becomes energetically favorable in the Mode-II region of Fig. 11(a). It is worth noting that, to the best of our knowledge, the transition from twinning in α-Mg to dislocation glide in LPSO during the interaction has not been previously observed in Mg alloys [54]. If a twin tip is crudely approximated by a pile-up of twinning dislocations [69], the thickness of the twin correlates more or less with the number of dislocations in the pile-up (assuming constant twin length). When twinning is impeded by a LPSO plate with the thickness larger than five building blocks, thicker twins tend to produce higher concentrated stresses at the twin/LPSO interface, which may lead to the plastic deformation of the LPSO plate by dislocation glide. With the thickness increase of the LPSO plate, the concentrated stresses at the twin tip may not be sufficient to initiate the plastic deformation and, instead, only elastic deformation of the LPSO plate. This leads to the transition of the LPSO response from plastic to elastic deformations, which, apparently, depends on the LPSO/twin thickness ratios and is described by the inclined boundary line between the Mode-II and the Mode-III regions in Fig. 11(a). With the LPSO plate thickness varying from ~5 nm to ~30 nm. On the basis of two critical experimental observations, i.e. the largest LPSO/twin thickness ratio of 0.16 of Mode-II and the smallest ratio of 0.18 of Mode-III, we adopted the average value of 0.17 ± 0.01 as the empirical

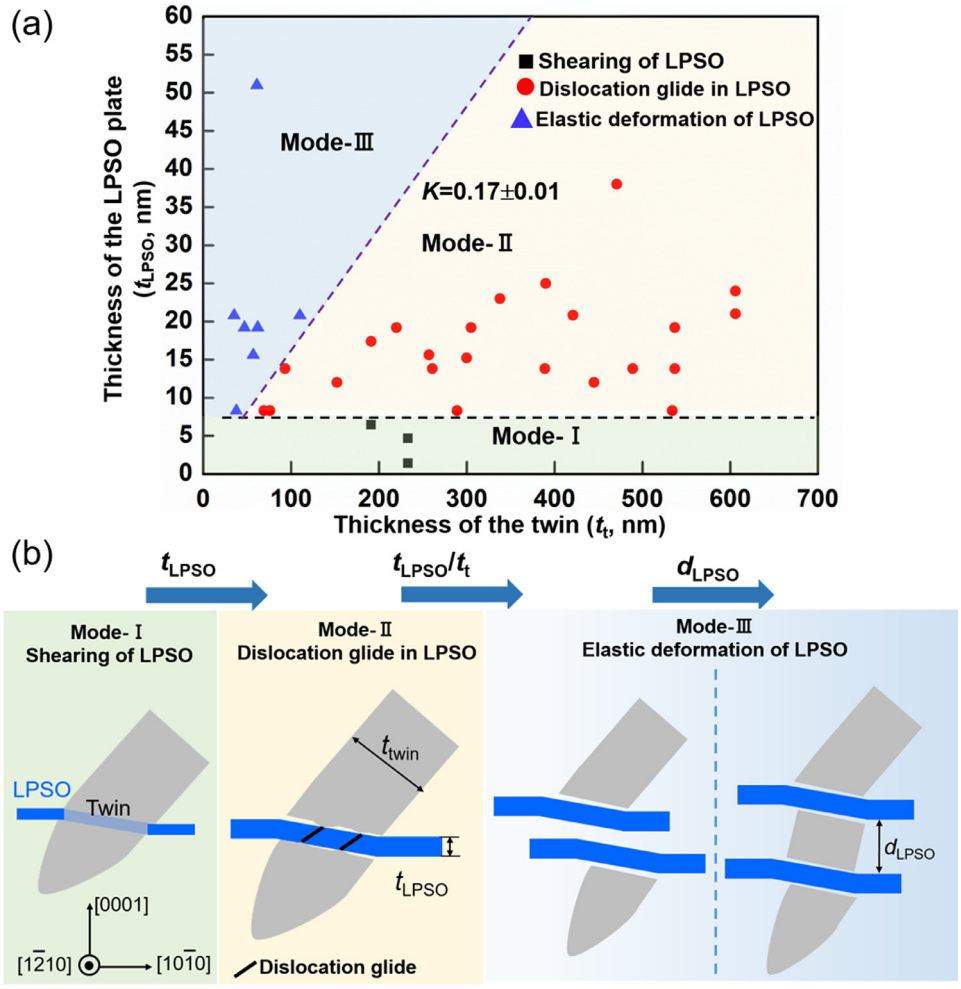

Fig. 11. (a) The dependence of {10-12} twin-LPSO interaction modes on the thicknesses of 14H LPSO plates and twins. (b) Schematic diagram showing the modes that {10-12} twins transmit through LPSO plates.

critical slope (Supplementary Fig. 4). Although this critical factor needs to be further verified by numerical simulations, the empirical criterion well describes the twin/LPSO interactions in our study with the common LPSO thicknesses ranging from several to tens of nanometres in Mg alloys [42,44]. It is highly possible that the empirical critical factor may not stand for LPSO plates with a large thickness over 50 nm. Since the thick 14H LPSO plates are very rare in the shock-loaded samples, we do not have sufficient data to specify this in the current study.

Based on our observations, the size-dependent interaction modes of {10$\bar{1}$2} twinning with 14H LPSO phase are summarized in Fig. 11 (b). The twin-LPSO interactions and thus precipitation strengthening of Mg alloys can be controlled by tailoring the thickness and inter-plate spacing of 14H LPSO. While the interaction mechanism proposed here is based on the results of {10$\bar{1}$2} twinning and 14H LPSO-type phase in the $Mg_{97}Zn_1Y_2$ alloy under shock loading, the general trend of the size-dependence (LPSO plate thickness, the thickness ratio between LPSO plates and deformation twins, and inter-plate spacing of precipitates) of {10$\bar{1}$2} twinning may be applicable to other types of LPSO phases or precipitates in Mg and other hcp alloys. Since the response of LPSO to twinning is not directly related with high strain rates, the interaction modes reported in this study should not limited to shock loading and, in principle, will be valid to quasi-static deformation of LPSO-reinforced Mg alloys. The findings from this study can also be implemented into nano-/atomic-scale physically based constitutive models for numerical simulations and predictions of mechanical behaviors of Mg alloys.

5. Conclusions

In summary, the interaction of {10$\bar{1}$2} twining with 14H LPSO phase in a $Mg_{97}Zn_1Y_2$ alloy has been systematically investigated using spherical aberration-corrected STEM. The main findings and conclusions are as follows:

1. The interaction modes of {10$\bar{1}$2} twins with LPSO plates depend on the thicknesses of LPSO plates and the thickness ratios between LPSO and twins.
2. Three response modes of 14H LPSO to {10$\bar{1}$2} twinning were characterized with atomic-scale observations: (1) twinning passing through a thin LPSO plate by direct shearing; (2) twin-to-dislocation 'switch' at the interfaces between α-Mg and LPSO; and (3) the discontinuous propagation of twinning facilitated by elastic deformation of thick LPSO plates.
3. Upon twin shearing, thin LPSO plates with a thickness not more than four building blocks experience pure shear deformation with the formation of a deformation zone which is in line with the incursive {10$\bar{1}$2} twin in structure and orientation. The shearing is accomplished by the structure transition of the fcc units in LPSO and direct twinning of the hcp components of LPSO.
4. When the LPSO plates have a thickness larger than four building blocks and the thickness ratios with twins are smaller than 0.17 ± 0.01, twinning cannot directly pass through the LPSO plates and there is a transition from twining in α-Mg to dislocation glide in LPSO.

5. When the LPSO/twin thickness ratios are larger than 0.17 ± 0.01, the incoming twins are fully stopped in front of a LPSO plate and the twinning is continued by the nucleation of a new twin near the opposite side of the LPSO/α-Mg interface accompanied by the elastic deformation of the LPSO plate.
6. In addition to the size dependence of twin and LPSO thicknesses, the propagation of $\{10\bar{1}2\}$ twining is also influenced by the interplate spacing of LPSO plates. The significant nano-size effect in the deformation modes of the α-Mg slats sandwiched between two LPSO plates can be observed, which is expected to affect the strengthening efficiency of LPSO precipitates.
7. On the basis of atomic-scale observations, the precipitation strengthening of Mg could be optimized by tailoring the size and spatial distribution of LPSO precipitates. Moreover, the systematical microstructure characterization also provides an experimental benchmark for designing and modeling new Mg alloys with improved mechanical properties.

Declaration of Competing Interest

We declare that we have no conflict of interest.

Acknowledgements

This work was sponsored by "World Premier International Research Center (WPI) Initiative" by MEXT, Japan. F. Z. is supported by JSPS postdoctoral program. M.C is sponsored by Whiting School of Engineering, Johns Hopkins University. B.L. thanks the support from US National Science Foundation (CMMI-1635088).

Supplementary materials

Supplementary material associated with this article can be found in the online version at doi:10.1016/j.actamat.2020.01.064.

References

[1] T.M. Pollock, Weight loss with magnesium alloys, Science 328 (2010) 986–987.
[2] K. Hono, C.L. Mendis, T.T. Sasaki, K. Oh-ishi, Towards the development of heat-treatable high-strength wrought Mg alloys, Scr. Mater. 63 (2010) 710–715.
[3] J.F. Nie, Precipitation and hardening in magnesium alloys, Metall. Mater. Trans. A 43 (2012) 3891–3939.
[4] Y. Kawamura, K. Hayashi, A. Inoue, T. Masumoto, Rapidly solidified powder metallurgy Mg97Zn1Y2 alloys with excellent tensile yield strength above 600 MPa, Mater. Trans. 42 (2001) 1172–1176.
[5] J.F. Nie, Y.M. Zhu, A.J. Morton, On the structure, transformation and deformation of long-period stacking ordered phases in Mg-Y-Zn alloys, Metall. Mater. Trans. A 45 (2014) 3338–3348.
[6] C. Bettles, M.R. Barnett, Advances in Wrought Magnesium Alloys: Fundamentals of Processing, Properties and Applications, Woodhead Publishing Limited, Cambridge UK, 2012.
[7] M.A. Meyers, Dynamic Behavior of Materials, John Wiley & Sons Inc., New York, 1994.
[8] J.W. Christian, S. Mahajan, Deformation twinning, Prog. Mater. Sci. 39 (1995) 1–157.
[9] M.A. Meyers, O. Vöhringer, V.A. Lubarda, The onset of twinning in metals: a constitutive description, Acta Mater. 49 (2001) 4025–4039.
[10] L. Wu, A. Jain, D.W. Brown, G.M. Stoica, S.R. Agnew, B. Clausen, D.E. Fielden, P.K. Liaw, Twinning-detwinning behavior during the strain-controlled low-cycle fatigue testing of a wrought magnesium alloy, ZK60A, Acta Mater. 56 (2008) 688–695.
[11] W. Wu, Y.F. Gao, N. Li, C.M. Parish, W.J. Liu, P.K. Liaw, K. An, Intragranular twinning, detwinning, and twinning-like lattice reorientation in magnesium alloys, Acta Mater. 121 (2016) 15–23.
[12] X.L. Liao, J. Wang, J.F. Nie, Y. Jian, P.D. Wu, Deformation twinning in hexagonal materials, MRS Bull. 41 (2016) 314–319.
[13] F. Siska, L. Stratil, J. Cizek, A. Ghaderi, M.R. Barnett, Numerical analysis of twin thickening process in alloys, Acta Mater. 124 (2017) 9–16.
[14] S.R. Niezgoda, A.K. Kanjarla, I.J. Beyerlein, C.N. Tomé, Stochastic modeling of twin nucleation in polycrystals: an application in hexagonal close-packed metals, Int. J. Plast. 56 (2014) 119–138.
[15] M.A. Gharghouri, G.C. Weatherly, J.D. Embury, The interaction of twins and precipitates in a Mg-7.7 at.% Al alloy, Phil. Mag. 78 (1998) 1137–1149.
[16] J.D. Robson, M.R. Barnett, The effect of precipitates on twinning in magnesium alloys, Adv. Eng. Mater. 21 (2019) 1800460.
[17] P.H. Manrique, J.D. Robson, M.T. Perez-Prado, Precipitation strengthening and reversed yield stress asymmetry in Mg alloys containing rare-earth elements: a quantitative study, Acta Mater. 4 (2017) 456–467.
[18] J.D. Robson, N. Stanford, M.R. Barnett, Effect of precipitate shape on slip and twinning in magnesium alloys, Acta Mater. 59 (2011) 1945–1956.
[19] J. Wang, N. Stanford, Investigation of precipitate hardening and slip twinning in Mg-5% Zn by micropillar compression, Acta Mater. 100 (2015) 53–63.
[20] J. Wang, M. Ramajayam, E. Charrault, N. Stanford, Quantification of precipitate hardening of twin nucleation and growth in Mg and Mg-5 Zn using micro-pillar compression, Acta Mater. 163 (2019) 68–77.
[21] C. Liu, P. Shanthraj, J.D. Robson, M. Diehl, S. Dong, J. Dong, W. Ding, D. Raabe, On the interaction of precipitates and tensile twins in magnesium alloys, Acta Mater. 178 (2019) 146–162.
[22] J.B. Clark, Age hardening in a Mg-9 wt.% Al alloy, Acta Metall. 16 (1968) 141–151.
[23] N. Stanford, J. Geng, Y.B. Chun, C.H.J. Davies, J.F. Nie, M.R. Barnett, Effect of plate shaped particle distributions on the deformation behaviour of magnesium alloy AZ91 in tension and compression, Acta Mater. 60 (2012) 218–228.
[24] J.B. Clark, Transmission electron microscopy study of age hardening in a Mg-5 wt.% Zn alloy, Acta Metall. 13 (1965) 1281–1289.
[25] N. Stanford, M.R. Barnett, Effect of particles on the formation of deformation twins in magnesium-based alloy, Mater. Sci. Eng. A 516 (2009) 226–234.
[26] J. Jain, P. Cizek, W.J. Poole, M.R. Barnett, The role of back stress caused by precipitates on $\{10\bar{1}2\}$ twinning in a Mg-6 Zn alloy, Mater. Sci. Eng. A 647 (2015) 66–73.
[27] G. Garces, J. Medina, P. Perez, K. Mathis, K. Horvath, A. Stark, N. Schell, P. Adeva, Influence of quasicrystal I-phase on twinning of extruded Mg-Zn-Y alloys under compression, Acta Mater. 151 (2018) 271–281.
[28] M. Matsuda, S. Ii, Y. Kawamura, Y. Ikuhara, M. Nishida, Interaction between long period stacking order phase and deformation twin in rapidly solidified $Mg_{97}Zn_1Y_2$ alloy, Mater. Sci. Eng. A 386 (2004) 447–452.
[29] X.H. Shao, Z.Q. Yang, X.L. Ma, Strengthening and toughening mechanisms in Mg-Zn-Y alloy with a long period stacking ordered structure, Acta Mater. 58 (2010) 4760–4771.
[30] J. Geng, Y.B. Chun, N. Stanford, C.H.J. Davies, J.F. Nie, M.R. Barnett, Processing and properties of Mg-6Gd-1Zn-0.6Zr part 2. Mechanical properties and particles twin interactions, Mater. Sci. Eng. A 528 (2011) 3659–3665.
[31] X.H. Shao, S.J. Zheng, D. Chen, Q.Q. Jin, Z.Z. Peng, X.L. Ma, Deformation twinning induced decomposition of lamellar LPSO structure and its re-precipitation in an Mg-Zn-Y alloy, Sci. Rep. 6 (2016) 30096.
[32] B.Y. Liu, N. Yang, J. Wang, M.R. Barnett, Y.C. Xin, D. Wu, R.L. Xin, B. Li, R.L. Narayan, J.F. Nie, J. Li, E. Ma, Z.W. Shan, Insight from in situ microscopy into which precipitate morphology can enable high strength in magnesium alloys, J. Mater. Sci. Technol. 34 (2018) 1061–1066.
[33] H.D. Fan, Y.X. Zhu, Jaafar A. El-Awady, D. Raabe, Precipitation hardening effects on extension twinning in magnesium alloys, Int. J. Plast. 106 (2018) 186–202.
[34] F.X. Wang, B. Li, Origin of deflection of precipitates during interaction with a migrating twin boundary in magnesium alloys, Comput. Mater. Sci. 154 (2018) 472–480.
[35] J.C.F. Millett, S.M. Stirk, N.K. Bourne, G.T. Gray III, On the behaviour of the magnesium alloy, AZ61 to one-dimensional shock loading, Acta Mater. 58 (2010) 5675–5682.
[36] P.J. Hazell, G.J. Appleby-Thomas, E. Wielewski, C. Stennett, C. Siviour, The influence of microstructure on the shock and spall behaviour of the magnesium alloy, elektron 675, Acta Mater. 60 (2012) 6042–6050.
[37] F. Zhang, M. Hao, F.C. Wang, C.W. Tan, X.D. Yu, H.L. Ma, H.N. Cai, Role of $\{10\bar{1}2\}$ twinning and detwinning in the shock-hardening behavior of rolled Mg-3Al-1 Zn alloy, Scr. Mater. 67 (2012) 951–954.
[38] G.T. Gray III, Influence of shock-wave deformation on the structure/property behavior of materials, in: J.R. Asay, M. Shahinpoor (Eds.), High Pressure Shock Compression of Solids, Springer-Verlag, New York, 1993, pp. 187–215.
[39] G.T. Gray III, Shock wave testing of ductile material, in: H. Kuhn, D. Medlin (Eds.), ASM Handbook Mechanical Testing and Evaluation, 8, ASM International, Materials Park, Ohio, 2000, pp. 462–476.
[40] F. Zhang, Y. Ren, S.C. Ning, Y. Tian, W.W. Hu, C.W. Tan, T. Fujita, A. Hirata, M.W. Chen, Deformation behaviour of 18R long-period stacking ordered structure in an Mg-Zn-Y alloy under shock loading, Intermetallics 102 (2018) 21–25.
[41] L.D. Marks, Wiener-filter enhancement of noisy HREM images, Ultramicroscopy 62 (1996) 43–52.
[42] Y.M. Zhu, A.J. Morton, J.F. Nie, The 18R and 14H long-period stacking ordered structures in Mg-Y-Zn alloys, Acta Mater. 58 (2010) 2936–2947.
[43] Y.M. Zhu, A.J. Morton, J.F. Nie, Growth and transformation mechanisms of 18R and 14H in Mg-Y-Zn alloys, Acta Mater. 60 (2012) 6562–6572.
[44] J.K. Kim, S. Sandlöbes, D. Raabe, On the room temperature deformation mechanisms of a Mg–Y–Zn alloy with long-period-stacking-ordered structures, Acta Mater. 82 (2015) 414–423.
[45] B. Xu, L. Capolungo, D. Rodney, On the importance of prismatic/basal interfaces in the growth of $(\bar{1}012)$ twins in hexagonal close packed crystals, Scr. Mater. 68 (2013) 901–904.
[46] C.D. Barrett, H.E. Kadiri, The roles of grain boundary dislocations and disclinations in the nucleation of $\{10\bar{1}2\}$ twinning, Acta Mater. 63 (2014) 1–15.
[47] B.Y. Liu, J. Wang, B. Li, L. Lu, X.Y. Zhang, Z.W. Shan, Twinning-like lattice reorientation without a crystallographic twinning plane, Nat. Commun. 5 (2014).
[48] J. Tu, S.Q. Zhang, On the $\{10\bar{1}2\}$ twinning growth mechanism in hexagonal close-packed metals, Mater. Design 96 (2016) 143–149.
[49] R.C. Pond, D.S. Vlachavas, Proc R Soc Lond A: Math Phys Sci 386 (1983) 95–143.

[50] J.P. Hirth, J. Lothe, Theory of Dislocations, 2nd ed., Wiley, New York, 1982.
[51] J.P. Hirth, R.C. Pond, Steps, dislocations and disconnections as interface defects relating to structure and phase transformations, Acta Mater. 44 (1996) 4749–4763.
[52] J.P. Hirth, R.C. Pond, R.G. Hoagland, X.Y. Liu, J. Wang, Interface defects, reference spaces and the Frank–Bilby equation, Prog. Mater. Sci. 58 (2013) 749–823.
[53] W.W. Hu, Z.Q. Yang, H.Q. Ye, <c+a>dislocations and their interactions with other crystal defects in a Mg alloy, Acta Mater. 124 (2017) 372–382.
[54] J.D. Robson, The effect of internal stresses due to precipitates on twin growth in magnesium, Acta Mater. 121 (2016) 277–287.
[55] J.W. Christian, The Theory of Transformations in Metals and Alloys, third ed., Pergamon Press, Oxford, 2002.
[56] M.R. Barnett, H. Wang, T.T. Guo, An orowan precipitate strengthening equation for mechanical twinning in Mg, Int. J. Plast. 112 (2019) 108–122.
[57] M.R. Barnett, N. Stanford, A. Ghaderi, F. Siska, Plastic relaxation of the internal stress induced by twinning, Acta Mater. 61 (2013) 7859–7867.
[58] M.A. Kumar, I.J. Beyerlein, R.J. McCabe, C.N. Tome, Grain neighbour effects on twin transmission in hexagonal close-packed materials, Nat. Commun. 7 (2016) 13826.
[59] L. Wang, Y. Yang, P. Eisenlohr, T. Bieler, M. Crimp, D. Mason, Twin nucleation by slip transfer across grain boundaries in commercial purity titanium, Metall. Mater. Trans. A 41 (2010) 421–430.
[60] L. Wang, P. Eisenlohr, Y. Yang, T. Bieler, M. Crimp, Nucleation of paired twins at grain boundaries in titanium, Scr. Mater. 63 (2010) 827–830.
[61] S.G. Song, G.T. Gray III, Structural interpretation of the nucleation and growth of deformation twins in Zr and Ti–I: application to the coincident site lattice theory to twinning problems in HCP structures, Acta Metall. Mater. 43 (1995) 2325–2337.
[62] S.G. Song, G.T. Gray III, Structural interpretation of the nucleation and growth of deformation twins in Zr and Ti–II: TEM study of twin morphology and defect reactions during twinning, Acta Metall. Mater. 43 (1995) 2339–2350.
[63] M.R. Barnett, Z. Keshavarz, A.G. Beer, D. Atwell, Influence of grain size on the compressive deformation of wrought Mg–3Al–1 Zn, Acta Mater. 52 (2004) 5093–5103.
[64] M.R. Barnett, A rationale for the strong dependence of mechanical twinning on grain size, Scr. Mater. 59 (2008) 696–698.
[65] K. Eswar Prasad, K. Rajesh, U. Ramamurty, Micropillar and macropillar compression responses of magnesium single crystals oriented for single slip or extension twinning, Acta Mater. 65 (2014) 316–325.
[66] G.D. Sim, G. Kim, S. Lavenstein, M.H. Hamza, H.D. Fan, Jaafar A. El-Awady, Anomalous hardening in magnesium driven by a size-dependent transition in deformation modes, Acta Mater. 144 (2018) 11–20.
[67] Y.T. Zhu, X.Z. Liao, X.L. Wu, Deformation twinning in nanocrystalline materials, Prog. Mater. Sci. 57 (2012) 1–62.
[68] Q. Yu, Z.W. Shan, J. Li, X.X. Huang, L. Xia, J. Sun, E. Ma, Strong crystal size effect on deformation twinning, Nature 463 (2010) 335–338.
[69] T.E. Mitchell, J.P. Hirth, The shape, configuration and stress field of twins and martensite plates, Acta Metall. Mater 39 (1991) 1711–1717.